RESEARCH OUTPUTS / RÉSULTATS DE RECHERCHE

Tuning Electronic and Morphological Properties for High-Performance Wavelength-Selective Organic Near-Infrared Cavity Photodetectors

Vanderspikken, Jochen; Liu, Quan; Liu, Zhen; Vandermeeren, Tom; Cardeynaels, Tom; Gielen, Sam; Van Mele, Bruno; Van den Brande, Niko; Champagne, Benoît; Vandewal, Koen; Maes, Wouter

Published in:
Advanced functional materials

DOI:
10.1002/adfm.202108146

Publication date:
2022

Link to publication

Citation for pulished version (HARVARD):
Vanderspikken, J, Liu, Q, Liu, Z, Vandermeeren, T, Cardeynaels, T, Gielen, S, Van Mele, B, Van den Brande, N, Champagne, B, Vandewal, K & Maes, W 2022, 'Tuning Electronic and Morphological Properties for High-Performance Wavelength-Selective Organic Near-Infrared Cavity Photodetectors', *Advanced functional materials*, vol. 32, no. 9, 2108146. https://doi.org/10.1002/adfm.202108146

Tuning Electronic and Morphological Properties for High-Performance Wavelength-Selective Organic Near-Infrared Cavity Photodetectors

Jochen Vanderspikken, Quan Liu,* Zhen Liu, Tom Vandermeeren, Tom Cardeynaels, Sam Gielen, Bruno Van Mele, Niko Van den Brande, Benoît Champagne, Koen Vandewal,* and Wouter Maes*

Incorporation of compact spectroscopic near-infrared (NIR) light detectors into various wearable and handheld devices opens up new applications, such as on-the-spot medical diagnostics. To extend beyond the detection window of silicon, i.e., past 1000 nm, organic semiconductors are highly attractive because of their tunable absorption. In particular, organic NIR wavelength-selective detectors have been realized by incorporating donor:acceptor thin films, exhibiting weak intermolecular charge-transfer (CT) absorption, into an optical microcavity architecture. In this work, the alkyl side chains of the well-known PBTTT donor polymer are replaced by alkoxy substituents, hereby redshifting the CT absorption of the polymer:PC$_{61}$BM blend. It is shown that the unique fullerene intercalation features of the PBTTT polymer are retained when half of the side chains are altered, hereby maximizing the polymer:fullerene interfacial area and thus the CT absorption strength. This is exploited to extend the detection range of organic narrow-band photodetectors with a full-width-at-half-maximum of 30–38 nm to wavelengths between 840 and 1340 nm, yielding detectivities in the range of 5×10^{11} to 1.75×10^{10} Jones, despite the low CT state energy of 0.98 eV. The broad wavelength tuning range achieved using a single polymer:fullerene blend renders this system an ideal candidate for miniature NIR spectrophotometers.

1. Introduction

Near-infrared (NIR) light detection using organic photodetectors (OPDs) allows to miniaturize surveillance, imaging, and spectroscopic devices, e.g., for medical applications such as functional brain imaging and the detection of viral diseases.[1–3] Organic semiconductor devices are potentially cheap, flexible, and light-weight due to their mild and easily scalable processing conditions on various substrates[4,5] and they can be directly integrated on complementary metal oxide semiconductor (CMOS) readout circuitry.[6,7] This allows for a facile miniaturization and implementation of this technology into handheld devices.[8] Broad-band photodetectors commonly utilize (ultra)low bandgap materials to detect lower energy NIR light.[9,10] However, the decreasing energy gap results in high dark currents and compromised detectivities.[11] For applications requiring narrow-band detection, several strategies have been proposed, including the use of narrow-band absorbers,[12] charge collection narrowing,[13] and resonant microcavity device architectures.[14] The latter is especially promising since such devices are electronically thin, yet optically thick at the resonance wavelength,[15,16] which is simply determined by the total thickness of the photoactive film and the transport layers sandwiched between the (semi)reflecting electrodes constituting the microcavity.[14]

Optical cavity devices have shown a broad wavelength tunability and applicability beyond 1000 nm by using the weak but

J. Vanderspikken, Q. Liu, T. Vandermeeren, T. Cardeynaels, S. Gielen,
K. Vandewal, W. Maes
Institute for Materials Research (IMO)
Hasselt University
Agoralaan, Diepenbeek 3590, Belgium
E-mail: quan.liu@uhasselt.be; koen.vandewal@uhasselt.be;
wouter.maes@uhasselt.be
J. Vanderspikken, Q. Liu, T. Vandermeeren, T. Cardeynaels, S. Gielen,
K. Vandewal, W. Maes
IMEC
Associated Lab IMOMEC
Wetenschapspark 1, Diepenbeek 3590, Belgium

Z. Liu, B. Van Mele, N. Van den Brande
Vrije Universiteit Brussel
Physical Chemistry and Polymer Science
Pleinlaan 2, Brussels 1050, Belgium

T. Cardeynaels, B. Champagne
University of Namur
Laboratory of Theoretical Chemistry
Theoretical and Structural Physical Chemistry Unit
Namur Institute of Structured Matter
Rue de Bruxelles 61, Namur 5000, Belgium

ADVANCED
SCIENCE NEWS
www.advancedsciencenews.com

ADVANCED
FUNCTIONAL
MATERIALS
www.afm-journal.de

broad charge-transfer (CT) absorption originating from intermolecular optical transitions at the interface of electron donor and acceptor type organic materials.[17] These transitions at photon energies below the optical gap of both the donor and acceptor have been extensively studied and have been linked to the open-circuit voltage in organic photovoltaics[18,19] as well as the minimum achievable dark current in OPDs.[11] In order to efficiently extend the detection window toward lower energy infrared light, two fundamental material design criteria need to be addressed. First, the intermolecular energy gap or CT state energy, approximated by the difference between the highest occupied molecular orbital (HOMO) of the donor and lowest unoccupied molecular orbital (LUMO) of the acceptor molecules, must be decreased to make lower energy sub-bandgap transitions available.[17,20] Second, the CT transitions must occur sufficiently frequent to achieve a threshold absorption coefficient for which cavity enhancement enables a reasonably high external quantum efficiency (EQE) at the resonance wavelength.[14] Since direct CT absorption is an intermolecular and thus inherently weak process, maximizing the amount of interface between the donor and acceptor is crucial. The most successful material system fulfilling these criteria to date is the intercalating system comprising poly[2,5-bis(3-tetradecylthiophen-2-yl)thieno[3,2-*b*]thiophene] (PBTTT) and [6,6]-phenyl-C_{61}-butyric acid methyl ester ($PC_{61}BM$),[21] which has shown its employability for cavity-enhanced NIR photodetection until 1000 nm. Extending the detection range to longer wavelengths was hampered due to the sharply decreasing CT absorption efficiency around 1.2 eV.[14]

The occurrence of conjugated polymers which, similar to PBTTT, allow intercalation of fullerene acceptors and other small molecules into their crystal structure is rather limited and highly dependent on the structural properties of the donor polymer.[22] So far, no structural alterations for solution-processable materials have been shown to decrease the CT state energy while maintaining a relatively high CT absorption strength at longer wavelengths. In this work, it is demonstrated that a novel side chain-engineered PBTTT-OR-R (alkoxy-alkyl) polymer is able to fulfil both the electronic and morphological blend requirements to extend the direct CT absorption to longer wavelengths. Additionally, it is shown that another side chain variant, the fully alkoxylated PBTTT-$(OR)_2$, does not yield the desired blend requirements. Using rapid heat-cool calorimetry (RHC) and X-ray diffraction (XRD) techniques, we find that the polymer for which half of the alkyl side chains are replaced by alkoxy counterparts maintains its (semi)crystalline and intercalating behavior. Fourier-transform photocurrent spectroscopy (FTPS) shows red-shifted, yet relatively strong CT absorption. When applied into a microcavity OPD, the PBTTT-OR-R:$PC_{61}BM$ devices are among the best-performing wavelength-tunable NIR OPDs with detectivities in the 1000–1340 nm wavelength range.

2. Results and Discussion

The intercalating nature of the PBTTT:$PC_{61}BM$ blend provides a large interfacial area between the donor and acceptor molecules and therefore rather efficient direct CT absorption. The synthetic challenge is therefore to design a polymer with

a high HOMO level which still allows $PC_{61}BM$ intercalation, hereby keeping the CT absorption coefficient rather high while pushing it further into the NIR. We hypothesized that (partial) substitution of the alkyl side chains of PBTTT for stronger electron-donating alkoxy side chains could allow to achieve this.[23] To estimate the influence of the replacement of alkyl by alkoxy side chains on the bithiophene moiety of PBTTT on the frontier orbital energy levels (in particular the HOMO), density functional theory (DFT) calculations (M06/6-311G(d)) were carried out (see the Supporting Information for details; Table S1, Supporting Information). The HOMO level of the pristine PBTTT ($HOMO_{calc}$: −4.95 eV) is predicted to significantly increase (by 0.37 eV) upon introduction of the oxygen atoms in the side chains ($HOMO_{calc}$ PBTTT-$(OR)_2$: −4.58 eV). The hybrid version, in which the bithiophene carries both an alkyl and an alkoxy side chain, has an intermediate value ($HOMO_{calc}$ PBTTT-OR-R: −4.88 eV).

These rationally designed polymers were subsequently synthesized. An overview of the synthesis pathways toward PBTTT and its novel variants is depicted in **Scheme 1**. Details of the synthesis of the thiophene precursors, 2-bromo-3-tetradecylthiophene (Th-R), and 2-bromo-3-(tetradecyloxy) thiophene (Th-OR), can be found in the Supporting Information. A palladium-catalyzed direct C−H coupling of Th-R and Th-OR yielded three bithiophene building blocks with increasing electron density.[24–26] Next to obtaining the previously reported alkyl (BiT-R_2) and alkoxy-substituted bithiophene (BiT-$(OR)_2$), the novel asymmetric alkyl-alkoxy-bithiophene (BiT-OR-R) was also obtained from a single reaction. Because of the significant increase in polarity that the oxygen atom brings to the bithiophene structure, the resulting mixture of three products was separated with relative ease using silica column chromatography. The polymers were subsequently prepared through palladium-catalyzed Stille cross-coupling polymerization (Scheme 1). The PBTTT polymer was made in a microwave reactor under similar conditions as originally reported by McCulloch et al.[27] For the polymerizations toward PBTTT-OR-R and PBTTT-$(OR)_2$, the catalytic system was changed to tetrakis(triphenylphosphine)palladium(0) and the polymerization was carried out using conventional heating. An overview of the obtained molar mass characteristics for the three polymers can be found in Table S2 (Supporting Information) (with the chromatograms in Figure S1, Supporting Information).

Thermogravimetric analysis (TGA) was carried out to judge the thermal stability of the polymers and to determine the upper temperature limit for thermal analysis by RHC (vide infra). All polymers showed an onset of degradation above 300 °C (Table S2, Supporting Information). The three polymers were subsequently analyzed by UV–vis–NIR absorption spectroscopy and cyclic voltammetry (CV) to get an estimate of the energy level shifts upon introduction of the alkoxy side chains. The introduction of alkoxy side chains shifts the wavelength (λ_{max}) at which the polymers have their maximum absorption in film. PBTTT has its maximum at 529 nm, while PBTTT-OR-R and PBTTT-$(OR)_2$ show a λ_{max} at 580 and 603 nm, respectively (Table S2 and Figure S2, Supporting Information). Absorption onsets are situated at 638, 675, and 715 nm for PBTTT, PBTTT-OR-R, and PBTTT-$(OR)_2$, respectively. The replacement of alkyl by alkoxy side chains does not strongly affect the LUMO
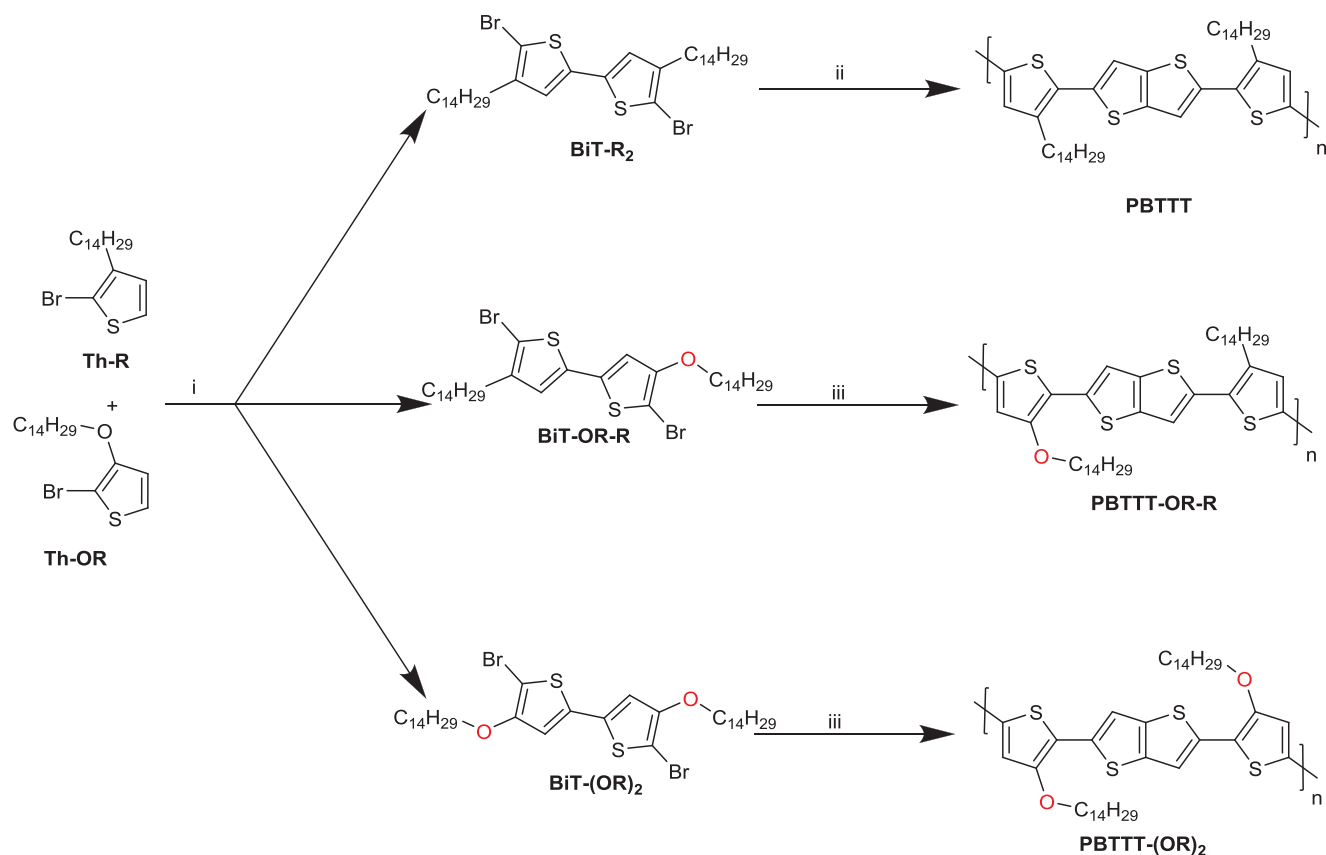
Scheme 1. a) Synthesis pathway toward PBTTT, PBTTT-OR-R, and PBTTT-(OR)$_2$: (i) AgNO$_3$, KF, Pd(PhCN)$_2$Cl$_2$, DMSO; (ii) 2,5-bis(trimethylstannyl)thieno[3,2-*b*]thiophene, Pd$_2$(dba)$_3$, P(*o*-tol)$_3$, chlorobenzene, μwave; (iii) 2,5-bis(trimethylstannyl)thieno[3,2-*b*]thiophene, Pd(PPh$_3$)$_4$, toluene/DMF.

energy level and almost exclusively influences the HOMO of the polymers (Table S2 and Figures S3 and S4, Supporting Information). Introduction of one alkoxy side chain results in a HOMO level increase of 0.25 eV (from −5.12 to −4.87 eV), while insertion of two alkoxy substituents shifts the HOMO upward by 0.42 eV (to −4.70 eV) as compared to PBTTT. While the absolute values of the estimated experimental HOMO levels differ from the calculated ones, the trend upon replacing alkyl by alkoxy side chains agrees reasonably well with the DFT calculations.

To determine the effect of side chain substitution on the optical CT transitions, bulk heterojunction blends of the polymers with PC$_{61}$BM were analyzed in an inverted photodiode stack ITO/ZnO/polymer:PC$_{61}$BM/MoO$_3$/Ag, which has a minimum of interference effects for thin photoactive layers (sample preparation details in the Supporting Information). In order to characterize the CT absorption band, the EQE spectra were measured with high sensitivity using FTPS[19] (**Figure 1**). The lower energy transitions are significantly more redshifted when using PBTTT-OR-R as compared to PBTTT as a consequence of the increased polymer HOMO level. The highest HOMO material, PBTTT-(OR)$_2$, has an even more extended CT absorption band. However, the overall EQE is about 3 times lower. Only at wavelengths longer than 1400 nm, PBTTT-(OR)$_2$ has a higher EQE than PBTTT-OR-R, but the EQE values remain very low (<0.05%) due to the very weak CT absorption in that spectral region.

The energy of the CT state onset, E_{CT}, was determined by fitting the CT absorption band onset with a Gaussian function derived from Marcus theory (Figure 1; and Table S2; fitting
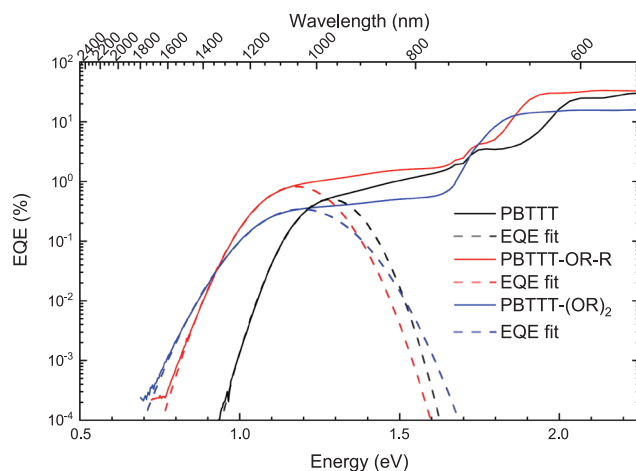
Figure 1. EQE spectra for PBTTT (black), PBTTT-OR-R (red), and PBTTT-(OR)$_2$ (blue) blends with PC$_{61}$BM in an inverted ITO device stack (glass/ITO/ZnO/active layer/MoO$_3$/Ag): EQE versus wavelength shows a significant extension of CT absorption to longer wavelengths due to the introduction of alkoxy side chains. EQE versus energy and the fitted curves (dashed black, red, and blue lines), illustrating decreasing E_{CT} gaps of 1.15, 0.98, and 0.89 eV for PBTTT, PBTTT-OR-R, and PBTTT-(OR)$_2$, respectively (see the Supporting Information for fitting details).

details in the Supporting Information).[28,29] E_{CT} significantly lowers from 1.15 eV for PBTTT:PC$_{61}$BM to 0.98 eV for the PBTTT-OR-R:PC$_{61}$BM system, i.e., a redshift of 0.17 eV, which is a bit less than the change in HOMO energy level estimated by CV (0.25 eV). Replacement of all alkyl by alkoxy side chains in PBTTT-(OR)$_2$ shifts E_{CT} by another 0.26 eV, affording 0.89 eV. Also this shift is lower than the estimated shift in HOMO energy levels (0.42 eV) determined by CV. This observation underlines once more that, while changes in frontier orbital energy levels will qualitativily agree with changes in CT state energies, it is hard to be quantitatively predictive. One should not forget that the frontier orbital energy levels are determined on the neat materials. As such, the electrostatic landscape at the interface and the CT state binding energy are not taken into account. Additionally, the CT absorption of the blend is broad and almost constant in the energy range 1.1–1.6 eV, which is rather unique. This is likely the result of a superposition of several possible types of CT transitions to higher energy electronic or vibrational states, each with a Gaussian(-like) line shape. As blend performance and detectivity parameters strongly depend on the morphology of the photoactive layer, the pristine polymers, PC$_{61}$BM, and their 1:1 mixtures (i.e., approximately the stoichiometric composition of the cocrystal) were analyzed by RHC as a probe for crystallinity (**Figure 2**). The pristine polymers all show side chain melting below 70 °C, followed by a liquid crystal transition in the case of PBTTT.[30] At elevated temperatures, all polymers exhibit a backbone melting (which is indicated in Figure 2 for PBTTT and PBTTT-OR-R by arrows). In the case of PBTTT-(OR)$_2$, a spread-out melting transition can be observed, which extends beyond the onset of degradation as determined by TGA, and was therefore not studied further. RHC measurements performed on the 1:1 mixtures indicate that a new melting peak is formed for PBTTT when mixed with PC$_{61}$BM at ≈230 °C, which is completely absent in the thermograms of the pristine components and has previously been attributed to melting of the co-crystal of PBTTT and PC$_{61}$BM.[22,31] A similar, albeit smaller new melting peak can be observed at ≈220 °C for the novel PBTTT-OR-R variant mixed with PC$_{61}$BM, which is again not present in the pristine components. For the PBTTT-(OR)$_2$ material, on the other hand, no new melting peak is observed when blended with PC$_{61}$BM. The RHC thermograms of the 1:4 mixtures (Figure S9, Supporting Information), as used for device preparation, show similar behavior as observed for the 1:1 mixtures, i.e., the appearance of a new melting peak at the same temperature as in the 1:1 mixtures for PBTTT and the novel PBTTT-OR-R variant mixed with PC$_{61}$BM, and no new melting peak for the PBTTT-(OR)$_2$:PC$_{61}$BM mixture. In addition, a new melting peak can now be observed originating from the excess of PC$_{61}$BM, preceded by its cold crystallization. An in-depth study of the full phase behavior of these systems falls outside the scope of the present work and will be the topic of a forthcoming publication.
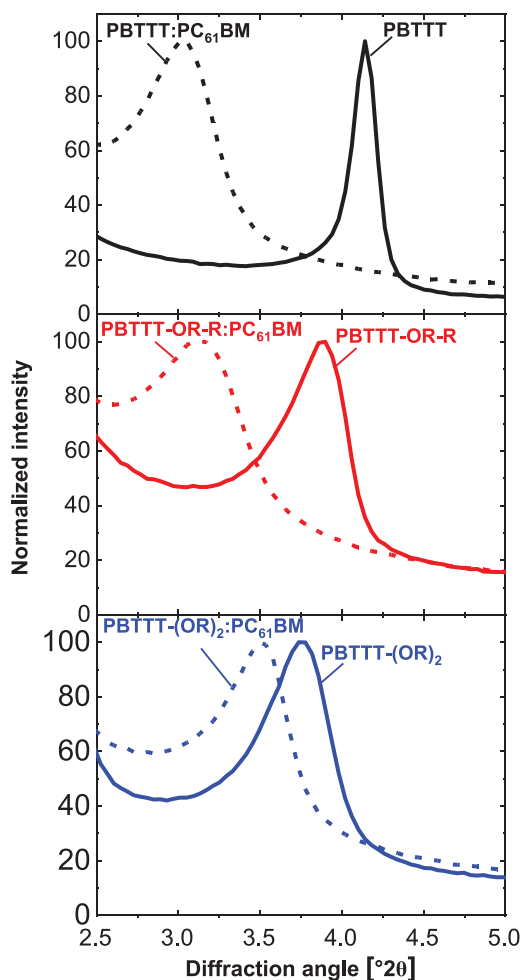
To further investigate, if the melting behavior observed for the novel materials is caused by intercalation of PC$_{61}$BM within the polymer crystallites, XRD analysis of the polymers and their blends was carried out (**Figure 3**). The d-spacing for the neat PBTTT polymer and its 1:1 mixture with PC$_{61}$BM amounts to 21.3 and 28.9 Å, respectively. This increase in d-spacing is consistent with literature[32] and has been attributed to the intercalation
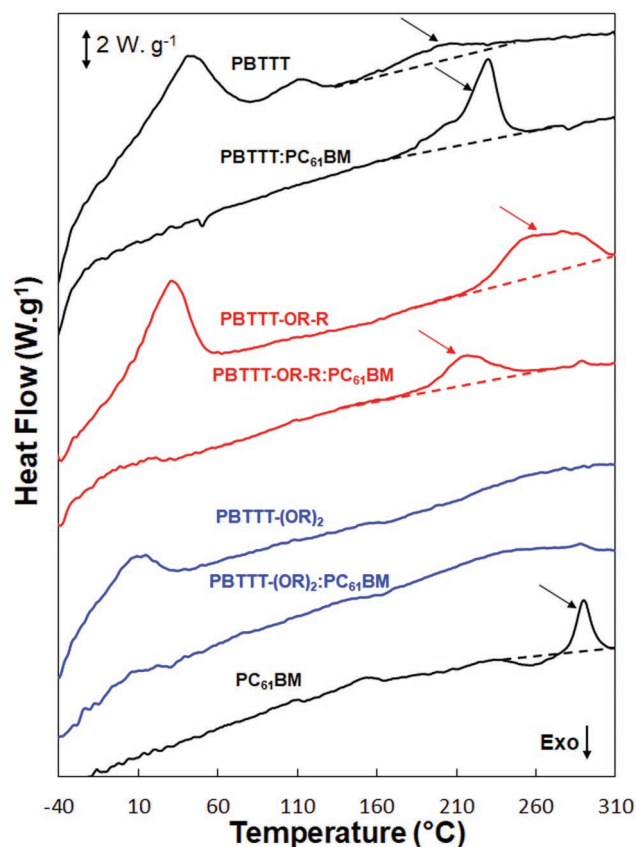
Figure 2. Rapid heat-cool calorimetry measurements (2nd heating) for the PBTTT polymer series, the respective 1:1 mixtures with PC$_{61}$BM, and pure PC$_{61}$BM. Arrows indicate the backbone melting of PBTTT and PBTTT-OR-R, the melting peak of PC$_{61}$BM, and the two new melting peaks observed for the 1:1 mixtures containing PBTTT and PBTTT-OR-R. The curves were vertically shifted for clarity.

of PC$_{61}$BM in between the PBTTT side chains, pushing the backbones further apart.[21,30,32] When looking at PBTTT-OR-R, also here the d-spacing increases significantly upon blending with PC$_{61}$BM, from 22.6 to 28.2 Å. For the PBTTT-(OR)$_2$ material, however, a minor increase from 23.4 to 25.3 Å is observed. These results suggest that intercalaction with PC$_{61}$BM is likely maintained for the PBTTT-OR-R material, while its presence is for sure less pronounced for the mixture containing PBTTT-(OR)$_2$. Further studies to get a deeper insight into the phase behavior of these novel blends, the optimal polymer:PC$_{61}$BM ratio for intercalation, and the origin of the reduction (or even complete absence) of intercalation in the PBTTT-(OR)$_2$:PC$_{61}$BM blend are ongoing. Nevertheless, current insights allow to explain why the sub-bandgap CT absorption is still significant for PBTTT-R-OR at lower energy wavelengths, as close mixing due to intercalation allows for a large interfacial area and a relatively efficient CT absorption.

To achieve a high-performance detector with a high specific detectivity (D^*), a low dark current density (J_D) is crucial. However, recent work has shown that for low E_{CT} devices ($E_{CT} < ≈0.9$ eV), the dark current becomes intrinsically limited by the photoactive material blend, exponentially increasing with decreasing E_{CT}.[11] **Figure 4** shows current density–voltage (J–V)

**ADVANCED
SCIENCE NEWS**

www.advancedsciencenews.com

**ADVANCED
FUNCTIONAL
MATERIALS**

www.afm-journal.de

Figure 3. X-ray diffraction patterns for the pristine polymers (solid lines) and 1:1 mixtures with $PC_{61}BM$ (dashed lines).

curves measured in the dark for the different polymer:$PC_{61}BM$ blends in inverted ITO-based device stacks for two different active layer thicknesses (device preparation details can be found
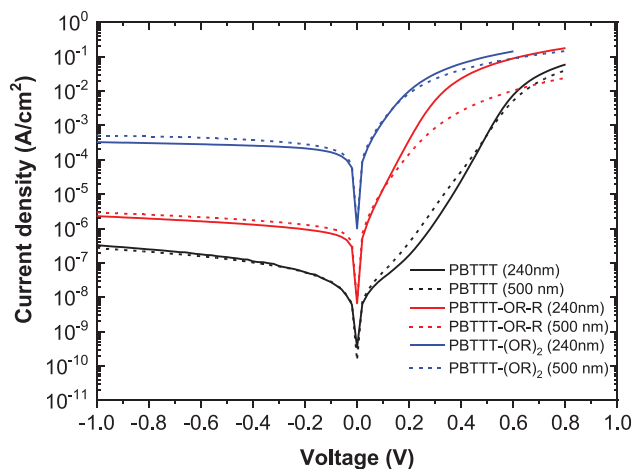
Figure 4. Dark current densities as a function of voltage obtained for PBTTT, PBTTT-OR-R, and PBTTT-$(OR)_2$ blends with $PC_{61}BM$ with a thickness of 240 and 500 nm in inverted ITO device stacks.

in the Experimental Section). For all three material systems, the J–V curves in the reverse voltage region do not depend strongly on the active layer thickness. However, a clear trend of the dark current with E_{CT} is observed. The lowest dark current is obtained for PBTTT:$PC_{61}BM$ and it increases about one order of magnitude for the PBTTT-OR-R blend and three orders of magnitude for PBTTT-$(OR)_2$:$PC_{61}BM$ (Figure 4).

A lower limit for the absolute value of the dark current density at reverse voltages can be calculated based on measurements of the absolute value of the photocurrent density (J_{Ph}) and open-circuit voltage (V_{OC}) of devices under illumination (experimental details in the Supporting Information)[11]

$$J_D > J_{Ph}e^{-V_{oc}\frac{q}{kT}} \tag{1}$$

For the PBTTT-OR-R and PBTTT-$(OR)_2$ devices, this corresponds to a lower limit to J_D of 5.7×10^{-7} and 1.1×10^{-4} A cm^{-2}, respectively. The measured J_D values at -1 V, 2.3×10^{-6} and 3.2×10^{-4} A cm^{-2}, respectively, are within a factor of 4 from these lower limits (**Table 1**). This indicates that, for these devices, the mechanisms determining J_D are similar to those limiting their V_{OC}, known to be intrinsic to the photoactive layer and resulting in a linear dependence of V_{OC} on E_{CT}.[11] Using this correlation in Equation (1), one finds indeed that J_D exponentially depends on E_{CT}, as previously reported for donor:acceptor blends with an E_{CT} in the range of 0.9 eV (or smaller).[11] For PBTTT:$PC_{61}BM$, we obtain a measured J_D at -1 V being much larger (by 5 orders of magnitude) than the lower limit calculated via Equation (1). This can be attributed to the presence of pinholes, traps and/or injection of charge carriers from the electrode contacts, causing additional dark current on top of the ideal diode dark current.[33] The dark current for this material blend is therefore not limited by intrinsic bulk properties. The ratio $J_D/J_{D,V_{OC}}$ will approach unity when the device is intrinsically limited by bulk properties and will be much larger than 1 when extrinsic factors are present (Table 1). For PBTTT, this ratio is in the order of 10^4, while PBTTT-OR-R and PBTTT-$(OR)_2$ show a value close to 1, indicating that the latter are more bulk-limited systems.

As the CT absorption is significantly extended to longer wavelengths for PBTTT-OR-R:$PC_{61}BM$ as compared to PBTTT:$PC_{61}BM$, while retaining similar EQE values in the CT band (Figure 1), this blend was used in an optical cavity device. PBTTT-$(OR)_2$:$PC_{61}BM$, on the other hand, was not further pursued due to the high (intrinsically limited) dark current and low EQE for this combination. The resonance wavelength of the Fabry–Pérot cavity is proportional to the effective refractive index of the photoactive layer and the thickness of the cavity.[34] Based on optical transfer matrix model simulations, the required blend thicknesses were estimated to achieve narrow-band resonances between 842 and 1340 nm (Figure S10, Supporting Information).[35] The optimized device stack consists of the active layer with ZnO as electron transport layer and MoO_3 as hole transport layer sandwiched between a nontransparant (thick) and a semitransparent (thin) Ag electrode on a glass substrate (see **Figure 5**a). Measured dark currents of the cavity devices are comparable to the dark currents observed in the optimized ITO devices (Figure S11, Supporting

**ADVANCED
SCIENCE NEWS**
www.advancedsciencenews.com

**ADVANCED
FUNCTIONAL
MATERIALS**
www.afm-journal.de

Table 1. Overview of the obtained E_{CT}, V_{OC}, J_{Ph}, and J_D values for the PBTTT polymer series blended with $PC_{61}BM$ in ITO devices and the calculated V_{OC}-limited dark current, $J_{D,V_{oc}}$, and the $J_D/J_{D,V_{oc}}$ ratio, showing the proximity for the three material blends to being intrinsically limited by bulk properties.

Material	E_{CT} [eV]	V_{OC} [V]	J_{Ph} [A cm^{-2}]	J_D (at −1 V) [A cm^{-2}]	$J_{D,V_{oc}}$ [A cm^{-2}]	$J_D/J_{D,V_{oc}}$
PBTTT	1.15	0.53	4.5×10^{-3}	3.0×10^{-7}	5.0×10^{-12}	6.0×10^4
PBTTT-OR-R	0.98	0.23	4.4×10^{-3}	2.3×10^{-6}	5.7×10^{-7}	4.0
PBTTT-(OR)$_2$	0.89	0.09	3.5×10^{-3}	3.2×10^{-4}	1.1×10^{-4}	2.9

Information). EQEs from 18.3% at 842 nm and 0.6% at 1340 nm were achieved with narrow peak responses with a full-width-at-half-maximum (FWHM) between 30 and 38 nm (Figure 5b,d, respectively). The cavity-based detectors still show a significant
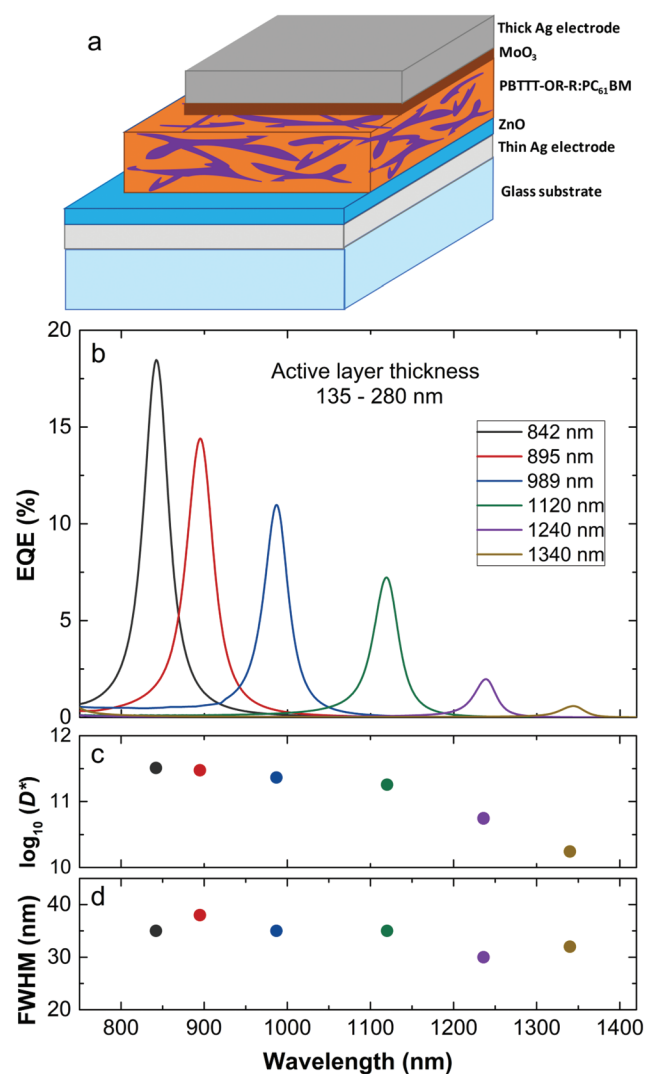
Figure 5. a) Schematic representation of the utilized device stack for the cavity photodetectors. b) EQEs of the metal–metal cavity device based on PBTTT-OR-R:$PC_{61}BM$ (1:4), with active layer thicknesses ranging from 135 to 280 nm. c) Obtained detectivities between 842 and 1340 nm. d) FWHM values of the resonance peaks.

response below 800 nm (Figure S12, Supporting Information), which can be supressed using a thin layer of PBTTT, as previously reported, without significantly hampering device performance.[14] Atomic force microscopy (Figure S13, Supporting Information) showed no clear signs of phase separation and a very low surface roughness for all active layers. The latter is of high importance to minimize fluctuations in the thickness of the cavity and to maintain a narrow detector response. From the current density–voltage response of these photodetectors, the shunt resistance (R_{sh}) at 0 V was extracted to be around 0.1 MΩ cm^2, rather independent of active layer thickness.[36] A lower limit to the noise current spectral density (j_{noise}, in units A Hz$^{-1/2}$ cm^{-1}) of the photodetector, taking shot and thermal noise into account, can be calculated using the following relationship

$$j_{noise} = \sqrt{2qJ_D + \frac{4k_bT}{R_{sh}}} \qquad (2)$$

with q the elementary charge and k_b the Boltzmann constant. When measured at short-circuit conditions, J_D will be zero and R_{sh} will determine the noise current. The calculated j_{noise} is similar for all devices, around 0.3 pA Hz$^{-1/2}$ cm^{-1}. The upper specific detectivity D^*, neglecting other noise sources such as $1/f$ noise, is calculated using

$$D^* = \frac{q\lambda EQE}{hcj_{noise}} \qquad (3)$$

where h is Planck's constant and c is the speed of light.[11,37] The corresponding D^* values range between 3.2×10^{11} and 1.7×10^{10} Jones and are among the highest reported detectivities for narrow-band OPDs (including CT absorption based cavity devices) between 1000 and 1340 nm (Figures 5c and 6). Structural manipulation through side chain engineering of the PBTTT polymer therefore expands the application window to longer wavelengths by significantly redshifting the weak direct CT transition. When compared to the best detectivities achieved for broad-band OPDs between 1120 and 1340 nm, these devices perform similarly (D^* within the same order of magnitude) and only a simple broad band PBTTT filter is required to achieve narrow response detectors (**Figure 6**; and Table S4, Supporting Information).

3. Conclusion

We have tuned the electronic and morphological properties of polymer:$PC_{61}BM$ blends through side chain manipulation in order to optimize the subbandgap charge-transfer transitions for application in microcavity organic near-infrared photodetectors. When partly replacing the alkyl side chains of PBTTT by alkoxy ones, the intercalating behavior of $PC_{61}BM$, the large donor:acceptor interfacial area, and the relatively strong CT absorption are maintained, as shown by RHC and XRD. At the same time, the higher HOMO energy level induced by the electron-donating side chains results in a significantly redshifted CT absorption as well as an unavoidable increase in dark current. The latter is, however, close to its lower limit on the order
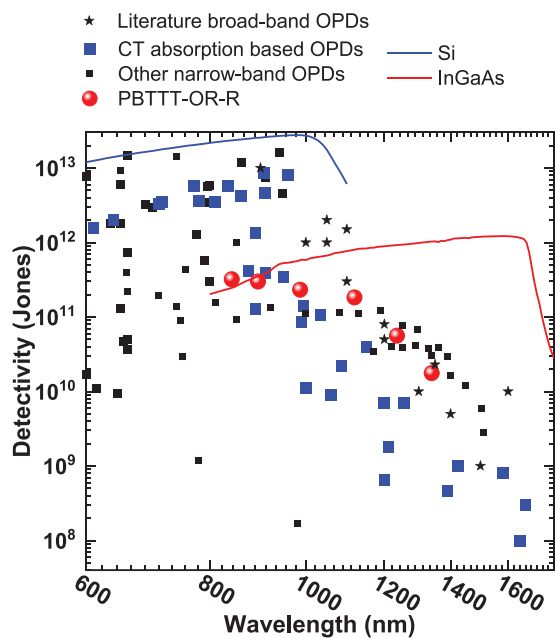
Figure 6. Comparison of the achieved performance for the PBTTT-OR-R cavity devices (red circles) to other CT absorption based cavity devices (blue squares), narrow-band (black squares), and broad-band photodetectors (black stars) (data in Table S4, Supporting Information). For the broad-band photodetectors, the best detectivity value at a certain wavelength was taken and detectivities were determined based on either measured or calculated noise currents. The thin blue and red colored lines represent commercial inorganic photodetectors.[38]

of 0.6 µA cm^{-2} for a donor:acceptor blend with an E_{CT} in the range of 0.9–1.0 eV. Incorporation into a microcavity device results in narrow-band organic photodetectors with a detection range extended by several hundreds of nm as compared to reference PBTTT:PC$_{61}$BM cavity detectors, with state-of-the-art specific detectivities observed between 1000 and 1340 nm. With a performance comparable to the best broad-band organic photodetectors in this spectral region, this type of devices additionally allows for a broad wavelength tunability and thus compact spectroscopic applications with a diagnostic window beyond 1000 nm and without the need for additional filtering, hereby providing great potential to be applied in the next-generation of portable and wearable smart devices.

4. Experimental Section

Materials and Methods: All reagents and chemicals were obtained from commercial sources and used without further purification. 2,5-Bis(trimethylstannyl)thieno[3,2-b]thiophene was synthesized according to a literature procedure.[39,40] Solvents were dried by a solvent purification system (MBraun, MB-SPS-800) equipped with alumina columns. Reactions under microwave irradiation were performed in a CEM Discover microwave.

NMR chemical shifts (δ, in ppm) were determined relative to the residual CHCl$_3$ proton signal (7.26 ppm) or the ^{13}C resonance shift of CDCl$_3$ (77.16 ppm). Polymer molar mass distributions were estimated by size exclusion chromatography (SEC) at 160 °C on an Agilent 1260 Infinity II high temperature GPC system using a PL-GEL 10 µm MIXED-B column with 1,2,4-trichlorobenzene as the eluent and using polystyrene internal standards. Background corrected UV–vis–NIR

absorption spectra were recorded on a Cary 5000 UV–vis–NIR spectrophotometer (Agilent) using a spectral band width of 2 nm. The optical gaps were estimated from the UV–vis–NIR-absorption spectra of the polymer films by introducing the wavelength at the intersection of the tangent line to the low energy side of the spectrum and the x-axis in the equation E_{gap} (eV) = 1240/wavelength (nm). CV was carried out in argon-purged acetonitrile at room temperature with an Autolab potentiostat (PGSTAT30 from Metrohm) controlled with GPES software (version 4.9) for data collection and data analysis. Tetrabutylammonium hexafluorophosphate (TBAPF$_6$) (0.1 M) was used as the supporting electrolyte. A one compartment microcell designed for three-electrode configuration was fitted with a platinum wire working electrode, a platinum wire counter electrode and an Ag/AgNO$_3$ reference electrode (Ag wire immersed in electrolyte containing 0.01 M AgNO$_3$). A film of the polymer analyte was formed on the working electrode by casting it from a chloroform solution. Voltammograms were recorded with a scan rate of 100 mV s^{-1} under a constant flow of argon, allowing degassing and blanketing of the electrolyte before and during analysis. Typically, 5 scans per film were recorded and HOMO/LUMO energy levels were estimated from the onset potentials of the third, fourth, and fifth scan. The onset potential was determined from the intersection of two tangents drawn at the rising and background current of the cyclic voltammogram. Ferrocene was used as an external standard. For calculation of the HOMO-LUMO energy levels the onset potential of oxidation/reduction, which is defined as the intersection of the linear extrapolation of the onset slope of the respective peak and the baseline, was used. For the conversion of potentials (V) obtained from the electrochemical measurements to molecular orbital energies (eV) the formal potential of the Fc/Fc$^+$ redox couple was scaled to the vacuum level with a value of –4.98 eV considering that 0.0 V on the Ferrocene scale corresponds to 0.31 V versus SCE (0.55 V vs SHE) and that 0.0 V versus SHE is equivalent to –4.44 eV.[41,42] The reported HOMO/LUMO values are averaged over scans 3, 4, and 5 of multiple experiments

HOMO/LUMO (eV) = –4.98 (eV) – E_{onset}(analyte) versus Ag/AgNO$_3$ (V) + E_f (Fc/Fc$^+$) versus Ag/AgNO$_3$ (V)

The accuracy of measuring redox potentials by CV is about 0.01–0.02 V. Reproducibility can be less because the potentials do depend on concentration and temperature.

TGA was performed on a TA instruments TGA Q5000. Measurements were performed at a heating rate of 20 K min^{-1} using nitrogen (25 mL min^{-1}) as the purge gas. Sample masses of ≈1 mg were used. The RHC used for this work is a prototype instrument developed by TA Instruments that allows a relatively wide range of heating and cooling rates up to 2000 K min^{-1}. Experiments were performed at a scanning rate of 500 K min^{-1} with nitrogen (6 mL min^{-1}) as the purge gas. Dedicated aluminum RHC crucibles were filled with around 200–250 µg of the respective polymer sample. A first heating was used to remove the thermal history and therefore all thermograms shown are from the second heating. XRD studies were performed with a Bruker D8 Discover using Cu Kα radiation. The samples were measured in θ–2θ scan mode using a parallel beam setup. The polymers or polymer:PC$_{61}$BM mixtures (6 mg mL^{-1}) were drop-casted from a solution in chlorobenzene at 80 °C onto a silicon substrate.

Device Preparation and Characterization: The sol–gel ZnO precursor (0.45 M) was prepared by dissolving zinc acetate dihydrate (Aldrich, 99.9%; 0.5 g) and ethanolamine (Aldrich, 99.5%; 0.14 g) in 2-methoxyethanol (Acros Organics, 99.8%; 5 mL). This solution was vigorously stirred at 60 °C for 2 h and then stirring was continued at room temperature overnight in air to complete the hydrolysis reaction. Solutions of polymer:PC$_{61}$BM (Solenne) at a total concentration of 25 or 50 mg mL^{-1} (donor:acceptor = 1:4 wt/wt in all the blends) were prepared in chloroform/o-dichlorobenzene (1.5/1, v/v) and stirred at 70 °C for 5 h in a N$_2$-filled glovebox before use. Standard ITO devices were fabricated using the inverted device structure glass/ITO/ZnO/active layer/MoO$_3$/Ag, whereas the cavity-OPDs were fabricated using the inverted device structure Eagle XG glass/Au (1.5 nm)/Ag (28 nm)/ZnO/active layer/MoO$_3$/Ag. For the interlayer study (Figure S6, Supporting Information), ZnO was substituted for PEIE [poly(ethylenimine), 80%

ethoxylated, 37 wt% in H_2O; Sigma-Aldrich], which was deposited by spin-coating with a layer thickness of ≈5 nm and then annealed at 100 °C for 10 min. Semitransparent thin Ag films were first fabricated by thermal evaporation ($<5 \times 10^{-6}$ mbar) with an extremely thin Au seed layer beneath.[43] The deposition rate for Au and Ag was 0.5 and 4 Å s^{-1}, respectively. Then, the ZnO precursor solution was spin-coated on the thin Ag electrodes at 4000 rpm and it was annealed at 150 °C in air for 20 min to form a 30 nm electron-transporting layer. The prepared samples were then transferred into a N_2-filled glovebox for spin-coating the active layer with varying thicknesses (140–500 nm) by adjusting the spin-casting rate and blend solution concentration. The blend thickness was monitored by a Bruker Veeco Dektak XT profilometer. The obtained EQE and dark currrent for the PBTTT-OR-R:$PC_{61}BM$ blend, as shown in Figures 1 and 3, was only achieved after slow drying the active layer of the spin-coated PBTTT-OR-R:$PC_{61}BM$ blend, which also has been shown to improve blend performance for PBTTT:$PC_{61}BM$ blends, supposedly due to better blend morphology.[21] The peak EQE was also increased by almost 10%, while the dark current decreased approximately one order of magnitude (Figure S8, Supporting Information). Finally, the MoO_3 (10 nm) hole-transporting layer and the Ag (100 nm) top electrode were sequentially deposited on top of the active layer through a shadow mask by thermal evaporation ($<5 \times 10^{-6}$ mbar) with an area of 0.06 cm^2. The freshly fabricated devices were measured in an inert atmosphere and light and dark J–V curves (forward scan with a step of 25 mV) were recorded using a Keithley 2400 Source Meter under AM1.5 1-sun illumination, provided by a solar simulator (Newport 91195A) with a silicon calibrated intensity equivalent to 100 mW cm^{-2}, and under dark, respectively. The EQE_{PV} spectrum for each cell was measured under chopped (135 Hz) monochromatic illumination from a Xe lamp (100 W, Newport) modulated by Cornerstone 130 Monochromator and an optical wheel chopper. The generated photocurrent from the solar cells was amplified with a Stanford Research System Model SR830 lock-in amplifier, and a calibrated Si photodiode with known spectral response was used as a reference. For the sensitive EQE measurements, an INVENIO R (Bruker Optics) with an external detector was employed. A low-noise current amplifier was used to amplify the photocurrent generated under illumination of the devices, with the illumination light modulated by the Fourier-transform infrared (FTIR) setup. AFM experiments were performed with a JPK NanoWizard 3 AFM (JPK Instruments AG, Berlin, Germany) using AC mode in air. Silicon ACTA-50 tips from AppNano with cantilever length ≈125 mm, spring constant ≈40 N m^{-1} and resonance frequency ≈300 kHz were used. The scan angle, set point height, gain values, and scan rate were adjusted according to the calibration of the AFM tip.

Supporting Information

Supporting Information is available from the Wiley Online Library or from the author.

Conflict of Interest

The authors declare no conflict of interest.

Data Availability Statement

The data that support the findings of this study are available from the corresponding author upon reasonable request.

[1] J. B. Balardin, G. A. Zimeo Morais, R. A. Furucho, L. Trambaiolli, P. Vanzella, C. Biazoli, J. R. Sato, *Front. Hum. Neurosci.* **2017**, *11*, 258.

[2] A. Sakudo, *Clin. Chim. Acta* **2016**, *455*, 181.

[3] M. S. Nogueira, *Photodiagn. Photodyn. Ther.* **2020**, *31*, 101892.

[4] R. D. Jansen-van Vuuren, A. Armin, A. K. Pandey, P. L. Burn, P. Meredith, *Adv. Mater.* **2016**, *28*, 4766.

[5] K. J. Baeg, M. Binda, D. Natali, M. Caironi, Y. Y. Noh, *Adv. Mater.* **2013**, *25*, 4267.

[6] H. Seo, S. Aihara, T. Watabe, H. Ohtake, T. Sakai, M. Kubota, N. Egami, T. Hiramatsu, T. Matsuda, M. Furuta, T. Hirao, *Jpn. J. Appl. Phys.* **2011**, *50*, 09MB04.

[7] S.-J. Lim, D.-S. Leem, K.-B. Park, K.-S. Kim, S. Sul, K. Na, G. H. Lee, C.-J. Heo, K.-H. Lee, X. Bulliard, R.-I. Satoh, T. Yagi, T. Ro, D. Im, J. Jung, M. Lee, T.-Y. Lee, M. G. Han, Y. W. Jin, S. Lee, *Sci. Rep.* **2015**, *5*, 7708.

[8] Z. Yang, T. Albrow-Owen, W. Cai, T. Hasan, *Science* **2021**, *371*, eabe0722.

[9] F. Verstraeten, S. Gielen, P. Verstappen, J. Raymakers, H. Penxten, L. Lutsen, K. Vandewal, W. Maes, *J. Mater. Chem. C* **2020**, *8*, 10098.

[10] F. Verstraeten, S. Gielen, P. Verstappen, J. Kesters, E. Georgitzikis, J. Raymakers, D. Cheyns, P. Malinowski, M. Daenen, L. Lutsen, K. Vandewal, W. Maes, *J. Mater. Chem. C* **2018**, *6*, 11645.

[11] S. Gielen, C. Kaiser, F. Verstraeten, J. Kublitski, J. Benduhn, D. Spoltore, P. Verstappen, W. Maes, P. Meredith, A. Armin, K. Vandewal, *Adv. Mater.* **2020**, *32*, 2003818.

[12] J. H. Kim, A. Liess, M. Stolte, A. Krause, V. Stepanenko, C. Zhong, D. Bialas, F. Spano, F. Würthner, *Adv. Mater.* **2021**, *33*, 2100582.

[13] A. Armin, R. D. Jansen-van Vuuren, N. Kopidakis, P. L. Burn, P. Meredith, *Nat. Commun.* **2015**, *6*, 6343.

[14] Z. Tang, Z. Ma, A. Sánchez-Díaz, S. Ullbrich, Y. Liu, B. Siegmund, A. Mischok, K. Leo, M. Campoy-Quiles, W. Li, K. Vandewal, *Adv. Mater.* **2017**, *29*, 1702184.

[15] Y. Wang, B. Siegmund, Z. Tang, Z. Ma, J. Kublitski, S. Xing, V. C. Nikolis, S. Ullbrich, Y. Li, J. Benduhn, D. Spoltore, K. Vandewal, K. Leo, *Adv. Opt. Mater.* **2021**, *9*, 2001784.

[16] J. Vanderspikken, W. Maes, K. Vandewal, *Adv. Funct. Mater.* **2021**, *31*, 2104060.

[17] C. Kaiser, K. S. Schellhammer, J. Benduhn, B. Siegmund, M. Tropiano, J. Kublitski, D. Spoltore, M. Panhans, O. Zeika, F. Ortmann, P. Meredith, A. Armin, K. Vandewal, *Chem. Mater.* **2019**, *31*, 9325.

[18] T. M. Burke, S. Sweetnam, K. Vandewal, M. D. McGehee, *Adv. Energy Mater.* **2015**, *5*, 1500123.

[19] K. Vandewal, K. Tvingstedt, A. Gadisa, O. Inganäs, J. V. Manca, *Nat. Mater.* **2009**, *8*, 904.

[20] B. Siegmund, A. Mischok, J. Benduhn, O. Zeika, S. Ullbrich, F. Nehm, M. Böhm, D. Spoltore, H. Fröb, C. Körner, K. Leo, K. Vandewal, *Nat. Commun.* **2017**, *8*, 15421.

**ADVANCED
SCIENCE NEWS**

www.advancedsciencenews.com

**ADVANCED
FUNCTIONAL
MATERIALS**

www.afm-journal.de

[21] N. C. Cates, R. Gysel, Z. Beiley, C. E. Miller, M. F. Toney, M. Heeney, I. McCulloch, M. D. McGehee, *Nano Lett.* **2009**, *9*, 4153.

[22] N. C. Miller, E. Cho, R. Gysel, C. Risko, V. Coropceanu, C. E. Miller, S. Sweetnam, A. Sellinger, M. Heeney, I. McCulloch, J. L. Brédas, M. F. Toney, M. D. McGehee, *Adv. Energy Mater.* **2012**, *2*, 1208.

[23] J. Lee, S.-J. Ko, H. Lee, J. Huang, Z. Zhu, M. Seifrid, J. Vollbrecht, V. V. Brus, A. Karki, H. Wang, K. Cho, T.-Q. Nguyen, G. C. Bazan, *ACS Energy Lett.* **2019**, *4*, 1401.

[24] M. A. M. Leenen, T. Meyer, F. Cucinotta, H. Thiem, R. Anselmann, L. De Cola, *J. Polym. Sci., Part A: Polym. Chem.* **2010**, *48*, 1973.

[25] M. Takahashi, K. Masui, H. Sekiguchi, N. Kobayashi, A. Mori, M. Funahashi, N. Tamaoki, *J. Am. Chem. Soc.* **2006**, *128*, 10930.

[26] K. Masui, H. Ikegami, A. Mori, *J. Am. Chem. Soc.* **2004**, *126*, 5074.

[27] I. McCulloch, M. Heeney, C. Bailey, K. Genevicius, I. MacDonald, M. Shkunov, D. Sparrowe, S. Tierney, R. Wagner, W. Zhang, M. L. Chabinyc, R. J. Kline, M. D. McGehee, M. F. Toney, *Nat. Mater.* **2006**, *5*, 328.

[28] K. Vandewal, K. Tvingstedt, A. Gadisa, O. Inganäs, J. V. Manca, *Phys. Rev. B* **2010**, *81*, 125204.

[29] R. A. Marcus, *J. Phys. Chem.* **1989**, *93*, 3078.

[30] N. C. Miller, R. Gysel, C. E. Miller, E. Verploegen, Z. Beiley, M. Heeney, I. McCulloch, Z. Bao, M. F. Toney, M. D. McGehee, *J. Polym. Sci., Part B: Polym. Phys.* **2011**, *49*, 499.

[31] F. C. Jamieson, E. B. Domingo, T. McCarthy-Ward, M. Heeney, N. Stingelin, J. R. Durrant, *Chem. Sci.* **2012**, *3*, 485.

[32] A. C. Mayer, M. F. Toney, S. R. Scully, J. Rivnay, C. J. Brabec, M. Scharber, M. Koppe, M. Heeney, I. McCulloch, M. D. McGehee, *Adv. Funct. Mater.* **2009**, *19*, 1173.

[33] K. Tvingstedt, C. Deibel, *Adv. Energy Mater.* **2016**, *6*, 1502230.

[34] M. S. Ünlü, S. Strite, *J. Appl. Phys.* **1995**, *78*, 607.

[35] L. A. A. Pettersson, L. S. Roman, O. Inganäs, *J. Appl. Phys.* **1999**, *86*, 487.

[36] A. Armin, M. Hambsch, I. K. Kim, P. L. Burn, P. Meredith, E. B. Namdas, *Laser Photon. Rev.* **2014**, *8*, 924.

[37] Y. Fang, A. Armin, P. Meredith, J. Huang, *Nat. Photonics* **2019**, *13*, 1.

[38] Thorlabs, Calibrated photodiodes, https://www.thorlabs.com/newgrouppage9.cfm?objectgroup_id=2822 (accessed: April 2021).

[39] X. Gong, M. Tong, Y. Xia, W. Cai, J. S. Moon, Y. Cao, G. Yu, C. L. Shieh, B. Nilsson, A. J. Heeger, *Science* **2009**, *325*, 1665.

[40] J. Tong, J. Li, P. Zhang, X. Ma, M. Wang, L. An, J. Sun, P. Guo, C. Yang, Y. Xia, *Polymer* **2017**, *121*, 183.

[41] A. J. Bard, L. R. Faulkner, *Electrochemical Methods: Fundamentals and Applications*, Hoboken, New Jersey, USA **2001**.

[42] S. Trasatti, *Pure Appl. Chem.* **1986**, *58*, 955.

[43] Q. Liu, L. G. Gerling, F. Bernal-Texca, J. Toudert, T. Li, X. Zhan, J. Martorell, *Adv. Energy Mater.* **2020**, *10*, 1904196.